ROYAL SOCIETY
OF CHEMISTRY

PAPER

CrossMark
click for updates

Nanostructured ZnFeZr oxyhydroxide precipitate as efficient phosphate adsorber in waste water: understanding the role of different material-building-blocks†

Michael Schneider,[ab] Asya Drenkova-Tuhtan,[c] Wojciech Szczerba,[de] Carsten Gellermann,[a] Carsten Meyer,[c] Heidrun Steinmetz,[f] Karl Mandel*[ab] and Gerhard Sextl[ab]

In the recent years great effort has been made to find materials and technologies for removing and recycling phosphate from waste water. We herein present the detailed study on a nanostructured multicomponent material, which turned out to be a very efficient phosphate adsorber. The role of each constituent is carefully examined to understand the collaborative interaction of the components of the nanostructured adsorber. We found evidence that it is particularly the nanostructure of this material, which has a crucial influence on the phosphate adsorption performance, indicating a synergetic effect of the different components. Moreover, the adsorption mechanism was studied dependent on the concentration of phosphate, changing from a Freundlich/Langmuir-like behaviour to a BET-like multilayer adsorption of phosphate on the material. Our work demonstrates that there is high potential for discovering new adsorber materials for environmental applications through careful engineering of the chemical composition in close connection with the materials (nano) structure.

Environmental significance

In recent years, great effort has been made to find new technologies to remove and recover phosphorus from wastewater. An elevated concentration increases the risk of eutrophication of the receiving water body. However, phosphorus is a non-renewable and irreplaceable resource, predominantly used as fertilizer in agriculture and needs to be recycled. Herein detailed investigations on the mechanism of phosphate uptake on a novel ZnFeZr based phosphate adsorber are conducted, leading to a better understanding of the role of the different components that make up this nanostructured material. This insight on the mechanism can be used to specifically create new adsorber materials for water purification and resources recovery, tackling one of the most important future topics in environmental science and technology.

1. Introduction

Currently, great effort is made to find technologies for the recycling of phosphorus from waste water. The reason is that

[a] *Fraunhofer Institute for Silicate Research, ISC, Neunerplatz 2, 97082 Wuerzburg, Germany. E-mail: karl-sebastian.mandel@isc.fraunhofer.de*
[b] *University of Wuerzburg, Chair of Chemical Technology of Materials Synthesis, Roentgenring 11, 97070 Wuerzburg, Germany*
[c] *University of Stuttgart, Institute for Sanitary Engineering, Water Quality and Solid Waste Management, Bandtaele 2, 70569 Stuttgart, Germany*
[d] *Academic Centre for Materials and Nanotechnology, AGH University of Science and Technology, al. Mickiewicza 30, 30-059 Kraków, Poland*
[e] *Bundesanstalt für Materialforschung und -prüfung (BAM), Unter den Eichen 87, 12205 Berlin, Germany*
[f] *University of Kaiserslautern, Department Resource Efficient Wastewater Technologies, Paul-Ehrlich-Str. 14, 67663 Kaiserslautern, Germany*
† Electronic supplementary information (ESI) available. See DOI: 10.1039/c6en00507a

on the one hand, phosphorus has to be removed during waste water treatment due to the risk of eutrophication in the receiving water body caused by algae bloom.[1,2] On the other hand, in the form of phosphate, it is one of the most important elements of life and builds up essential molecules such as the backbone of DNA and the energy carriers adenosine triphosphate (ATP) and adenosine diphosphate (ADP). Therefore it is an irreplaceable, valuable resource predominantly used as fertilizer in modern agriculture.[3] Furthermore, rock-phosphate, the main source of phosphorous, is a non-renewable and limited resource and because of the increasing demand, the natural deposits are depleted more and more.[4]

A promising approach to remove and recover P from waste water is the use of adsorber materials. Especially at low concentrations (µg L^{-1}–mg L^{-1}), adsorption is one of the most

This journal is © The Royal Society of Chemistry 2017

effective techniques for the removal of dissolved substances.[5] In the last decades, considerable work has been conducted in the area of synthesis and application of new adsorbers for phosphate. Recent research reports materials such as iron oxyhydroxides,[6–8] bimetal ferrites,[9] zirconium hydroxide,[10,11] aluminium hydroxide,[12,13] alunite,[14] functionalised mesoporous polymers,[15,16] lanthanum oxide,[17] lanthanum doped materials[18,19] and several variations of layered double hydroxides[20–23] as adsorbers for phosphate. The challenge is not only to develop a highly efficient adsorber for phosphate removal, but also to recover phosphate for reuse, for instance, as fertiliser.

Recently, we reported on a promising material created from the elements Zn, Fe and Zr which in a screening study[24] turned out to be the most promising candidate with respect to P adsorption among many other metal hydroxides tested. We also succeeded in depositing the material on magnetic carrier particles.[25] Removal and recovery of the adsorber by the aid of magnetic particles *via* magnetic separation is an elegant approach, replacing classical techniques such as the time consuming and discontinuous filtration. The adsorber material proved empirically its high potential during numerous repetitions of P adsorption and desorption in laboratory and pilot scale. However, the role of the different constituents is not understood yet. In this work, the phosphate uptake by the novel ZnFeZr based adsorber material is investigated in detail through a screening procedure, leading to a better understanding of the role of the different components that make up this nanostructured material.

2. Experimental

2.1 Reagents and materials

Zinc chloride ($ZnCl_2$), sodium hydroxide (NaOH) and hydrochloric acid (HCl, 36 wt%) were purchased from Carl Roth (Germany). Iron(II) chloride tetrahydrate ($FeCl_2 \cdot 4H_2O$), iron(III) chloride hexahydrate ($FeCl_3 \cdot 6H_2O$), zirconium(IV) oxychloride octahydrate ($ZrOCl_2 \cdot 8H_2O$) and sodium hydrogen phosphate (Na_2HPO_4) were purchased from Sigma-Aldrich (Germany). Nitric acid (HNO_3, 1 M, diluted from a 53 wt% solution), ammonia hydroxide solution (NH_3 (aq), 25 wt%) in water were purchased from Fischar Chemicals and used without further purification.

2.2 Precipitation of metal (Zn/Fe/Zr) oxyhydroxides for phosphate adsorption

The synthesis of the metal oxyhydroxides is based on a published procedure.[22,24,26] The precursor solution of the different samples was prepared by dissolving the desired amount of the three different metal salts of zinc, iron and zirconia in 100 mL of deionized water. The obtained solution was then added dropwise to 400 mL of 0.15 M NaOH solution in a 1 L round flask under stirring (300 rpm) within 10 min, maintaining a pH-value of pH > 10 the whole time to ensure that all metals were precipitated as oxides or hydroxides re-

spectively. The resulting suspension was stirred for additional 5 min and afterwards the pH was adjusted to 7 with concentrated hydrochloric acid to simulate the natural waste water environment. This step is important to avoid subsequent potential dissolution of metal cations when the structures are added to waste water, which normally has a pH of approximately 7–8. After neutralization, the samples were centrifuged, washed twice with deionized water and dispersed in deionized water. A fraction of each sample was dried at 80 °C, analysed with X-ray diffraction (XRD) and scanning electron microscopy (SEM) and used for the determination of the BET surface area.

2.3 Phosphate adsorption tests in phosphate spiked deionised water

To qualitatively verify the successful phosphate adsorption on the materials, Fourier transformed infrared spectroscopy (FTIR) measurements were conducted. For phosphate uptake, the sample materials were mixed with sodium hydrogen phosphate spiked deionised water (PO_4-P concentration: 100 mg L^{-1}). After 5 h of stirring the samples were separated by centrifugation, washed with deionised water once to remove the non-adsorbed phosphate and dried throughout 1 d at 75 °C. Subsequently, the samples were ground to fine powder.

Adsorption kinetics. For the determination of the adsorption kinetics, experiments were carried out with an initial phosphate concentration of approximately 10 mg L^{-1} PO_4-P in spiked deionised water and with a pH-value of 7–8. The amount of adsorber was set to 200 mg L^{-1} and the adsorption time was varied stepwise from 1 to 60 min. The solid–liquid separation was performed with a laboratory centrifuge and the supernatant was filtered through a 0.45 μm membrane filter. The remaining dissolved phosphate in the filtrate was determined with inductively coupled plasma optical emission spectroscopy (ICP-OES) measurements. The experimental data was analysed with pseudo-first-order and pseudo-second-order kinetic models. The equations of pseudo-first-order (1) and pseudo-second-order (2) can be expressed in a linear form as follows:

$$\lg\left(q_e - q_t\right) = \lg q_e - \frac{k_1}{2.303}t \tag{1}$$

$$\frac{t}{q_t} = \frac{1}{k_2 q_e^2} + \frac{t}{q_e} \tag{2}$$

where the rate constants for pseudo-first-order and pseudo-second-order kinetic models are k_1 (1/min) and k_2 (g mg^{-1} min), respectively. The amounts of phosphate adsorbed at equilibrium and at time t (min) are expressed as q_e and q_t (mg g^{-1}).

Adsorption isotherms. The experiments for the determination of the adsorption isotherms were carried out in the same

This journal is © The Royal Society of Chemistry 2017

Environ. Sci.: Nano, 2017, **4**, 180–190 | 181

manner like the kinetics experiments, *i.e.* with an initial phosphate concentration of approximately 10 mg L^{-1} PO$_4$-P in spiked deionised water and a pH-value of 7–8. The amount of adsorber was varied by applying concentrations from 10 to 2000 mg L^{-1}. The experiments were carried out with different volumes of phosphate solution depending on the adsorber concentration. The adsorber concentrations and the corresponding batch sizes can be seen in Table 1.

During adsorption, the suspensions were mixed with a magnetic stirrer (650 rpm) at room temperature for 4 h until adsorption equilibrium was reached. For sampling, the subsequent processes were conducted as described in the kinetics experiments.

The experimental data was analysed with Freundlich, Langmuir and BET models. The equations of Freundlich (3), Langmuir (4) and BET (5) can be expressed in the following linear form:

$$\ln q_e = \ln K_F + n \cdot \ln C_e \tag{3}$$

$$\frac{C_e}{q_e} = \frac{1}{K_L q_{max}} + \frac{1}{q_{max}} \cdot C_e \tag{4}$$

$$\frac{C_e}{q_e \cdot (C_0 - C_e)} = \frac{1}{K_{BET} q_{max}} + \frac{K_{BET}^{-1}}{K_{BET} q_{max}} \cdot \frac{C_e}{C_0} \tag{5}$$

where the sorption coefficient for Freundlich, Langmuir and BET models are K_F ((mg g^{-1})/(mg L^{-1})^n), K_L (L mg^{-1}) and K_{BET}, respectively. The phosphate uptake capacity and the concentration of dissolved phosphate at equilibrium are expressed as q_e (mg g^{-1}) and C_e (mg L^{-1}). The maximum concentration of phosphate in one layer is expressed as q_{max} (mg g^{-1}) and n is a constant.

The Freundlich and Langmuir model fits were applied with only using experimental data at low equilibrium concentrations between C_e = 0–8 mg L^{-1}, whereas the BET model fit was performed by using the complete set of experimental data.

2.4 Analytical instrumentation

The investigations on the morphology of the materials as well as the energy-dispersive X-ray spectroscopy (EDX) measurements were performed with a scanning electron microscope (SEM) using a Zeiss Supra 25 SEM at 3 keV (field emission). X-ray diffraction (XRD) was performed on dried powder samples of the investigated materials. A PANalytical 943006003002 Empyrean Series 2 X-ray diffractometer employing Cu Kα radiation (λ = 0.15406 nm) was used (step

size 0.00165 2θ, typical count time 60 s). The indication of reflections was carried out referring to the International Centre for Diffraction Data PDF-4. The chemical composition of the precipitated materials (after digesting the samples in hydrochloric acid), as well as the phosphate concentrations of the adsorption experiments were analysed with inductively coupled plasma optical emission spectroscopy (ICP-OES) using a Varian Vista-Pro CCD simultaneous ICP-OES. Specific surface areas were measured by N$_2$ adsorption using BET analyses following DIN66131 with a Quantachrome Instruments Autosorb-3B on degassed and dried samples (110 °C, 10^{-3} mbar, 16 h). Fourier transformed infrared spectroscopy (FTIR) was performed using a Nicolet Magna-IR 760 Spectrometer E.S.P. The samples were analysed as KBr pellets. The X-ray absorption fine structure (XAFS) experiment was carried out at BAMline experimental station of BESSY II lightsource, Berlin, Germany. The XAFS spectra were recorded in transmission mode at the K-edges of Fe, Zn and Zr. The data treatment and analysis was done using the Ifeffit software package.[27]

3. Results and discussion

3.1 Characterisation of the synthesised phosphate adsorbers

We recently learned that an empirically found mixture of the elements Zn, Fe and Zr in a certain combination turned out to be a highly efficient phosphate adsorber in waste water. However, there has been a lack of knowledge about the adsorption mechanism of the material. To gain a thorough understanding, the developed approach was to systematically vary the combination of the constituents in terms of molar ratio during co-precipitation and study the correlation between composition, structure and adsorption behaviour. Table 2 lists the combinations that were prepared for that purpose.

The "standard" material (sample 1) is the combination we found in our previous work as performing exceptionally well in phosphate adsorption. It has a rather complex structure and consists of crystalline zinc oxide nanoparticles embedded in an amorphous network containing Zn-, Fe- and Zr-ions in the form of oxyhydroxides. Starting from the standard sample 1, the influence of zinc was examined by either lowering (sample 2) or increasing (sample 3) its content. The ratio between iron and zirconia was kept constant for samples 2 and 3. For samples 4 and 5, the ratio between iron and zirconia was varied, while the molar ratio to zinc was kept the same as for the standard sample 1. For sample 6 only zinc-ions were used as precursor. Therefore, this sample was designed to mimic the crystalline ZnO-part of the standard. In the same manner, sample 7 was prepared by only using

Table 1 ZnFeZr adsorber concentration and respective batch volume for the phosphate adsorption tests in spiked deionised water

ZnFeZr adsorber concentration [mg L^{-1}]	10	20	35	50	100	200	350	500	1000	2000
Batch volume [ml]	1000	1000	1000	500	500	250	250	250	50	50

Table 2 Initial molar ratios of the used metal precursors for the investigated 8 samples, deviations relative to the reference/standard sample 1, and a graphical depiction for convenience and to ease the comparative discussion among all samples

Sample	Initial molar ratio of the precursor ions			Variation with respect to the standard combination	Graphical depiction
	Zn^{2+}	Fe^{3+}	Zr^{4+}		
1	6.0	1.0	1.0	This is the **standard**	
2	4.0	1.0	1.0	lower amount of Zn	
3	10.0	1.0	1.0	higher amount of Zn	
4	3.6	0.2	1.0	higher Zr, lower Fe	
5	18.0	5.0	1.0	higher Fe, lower Zr	
6	1.0	--	--	Zn component only	
7	--	1.0	1.0	Fe and Zr components only	
8	6.0	1.0	1.0	Post-synthesis mixture of 6 and 7	

iron- and zirconia-ions as precursor to mimic the amorphous part. It has to be considered that the material of sample 7 only approximately matches the amorphous part of the standard, which also incorporates zinc oxyhydroxides in its amorphous fraction. However, it is not possible to use mixtures with zinc ions in this co-precipitation process without the appearance of crystalline zinc oxide in the resulting material. In order to investigate whether it is important to do a co-precipitation of the three used metal salts to yield a high performance material, one last sample was created. Therefore sample 8 was prepared by mixing samples 6 and 7 in a way that the molar ratio of the metal ions used was similar to the standard.

For convenience and to ease the comparative discussion between all samples, a graphical depiction is also introduced in Table 2 and used in all figures where more than one sample is described. Zinc is represented by blue colour, iron is represented by red colour and zirconia is represented with grey colour in a bar graph. The length of the respective bar represents the molar amount of metal precursor used.

To verify the chemical composition of the examined materials, the samples were analysed by means of ICP-OES (Table 3). All precipitated materials contained the same molar ratio as offered for precipitation, *i.e.* the precipitation to solids from the metal precursors was complete in all cases. The only exception is the amount of Zn found by ICP-OES measurements which is lower compared to the initially used amount in nearly all cases. The co-precipitation is done in alkaline ammonia solution. Zinc compounds such as zinc oxide or zinc hydroxide behave amphoteric and therefore dissolve in basic environment. Hence, a potential reason for the loss of zinc is that zinc compound was washed out during the washing steps as long as it was not completely surrounded and protected by the amorphous network.

Since the samples shall be used as adsorbers, knowledge about their specific surface area is very important with re-

Table 3 Chemical composition of the investigated samples analysed with ICP-OES measurements and surface area of the samples 1–7 analysed by gas adsorption measurements using the BET-method

Sample	Molar ratios of the precursor ions by ICP-OES measurements			Surface area [$m^2\ g^{-1}$]
	Zn^{2+}	Fe^{3+}	Zr^{4+}	
1	5.3	1.0	1.0	115
2	3.2	1.0	1.0	135
3	9.1	1.0	1.0	80
4	3.3	0.2	1.0	90
5	15.2	5.2	1.0	125
6	1.0	—	—	10
7	—	1.0	1.0	335
8	6.0	1.0	1.0	—

spect to a subsequent comparison of the materials performance. Therefore, the specific surface area obtained from gas adsorption measurements using the BET-method is added to Table 3.

By comparing the samples 1, 2 and 3, it can be seen that an increased presence of Zn decreases the BET-surface area of the material. With an increase of Zn content, more zinc based crystalline material, such as zinc oxide, is formed upon precipitation (see below), which leads to the decrease of BET-surface as amorphous structures typically possess higher BET surfaces than crystalline material. This complies with the result obtained from sample 6, where the material is composed of precipitated Zn (crystalline ZnO) alone. For this sample the surface area is approximately 90% lower than the surface area of the standard sample. Furthermore, the following trends were found from BET-analysis: an increase in Zr-content (sample 4) leads to lower surface areas, whereas with the increase in Fe-content (sample 5), a higher surface area is obtained (a clear explanation for this trend was not found within the scope of this research). Finally, by removing Zn completely (sample 7), the highest specific surface area was

measured, with an increase of about 200% in comparison to the standard.

XRD-measurements. For further characterisation of the samples 1–7, the dried powders were analysed with X-ray diffraction measurements (Fig. 1). The standard sample (sample 1) only yields peaks from crystallites that can be assigned to ZnO (marked with "*"). Apparently, the constituents Fe and Zr are precipitated in an amorphous state only. The increase of Zn content (sample 3) leads to slightly sharper peaks that indicate ZnO. A decrease of the Zn content (sample 2) leads to the evolution of another series of peaks marked with "◊" that can be attributed to $Zn(OH)_2$. By increasing the amount of zirconia in the material (sample 4), the peaks indicating zinc hydroxide are more prominent. An increase of iron in the material (sample 5) does not lead to a significant change of the XRD-spectra, which means that the crystalline parts of the material do not differ from sample 1. Finally, samples 6 and 7 which were designed to mimic the crystalline (ZnO) and the amorphous part of the standard sample show the expected results for XRD-measurements. Sample 6 shows the prominent ZnO peaks indicating crystalline ZnO-particles, whereas in the diffractogram of sample 7, there is no prominent peak detectable which confirms the amorphous nature of this sample. Sample 8 was not analysed with XRD measurements since it is a mixture of samples 6 and 7.

The XRD analysis showed that only zinc in the form of zinc oxide and zinc hydroxide can be detected as crystalline phase. However, with ICP-OES measurements, all constituents (Zn, Fe and Zr) were found. Therefore, investigations by SEM and EDX were conducted to further reveal the structural composition of the samples.
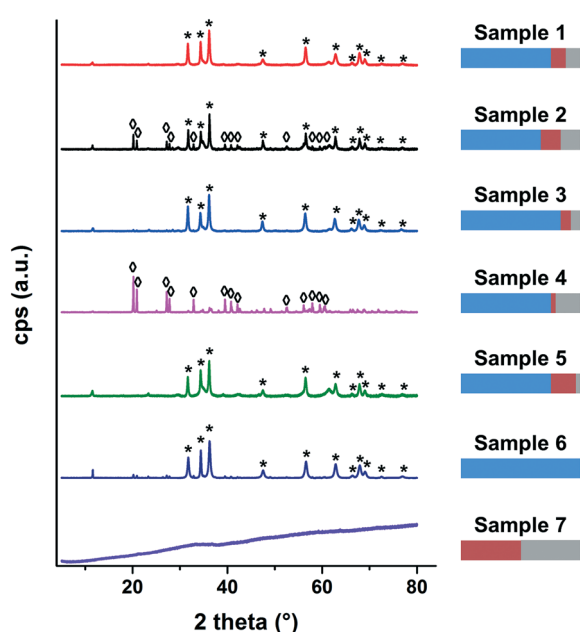
SEM and EDX measurements. The SEM-images of the samples 1–5 (Fig. 2) have a comparable granular appearance indicating the presence of small particles. These particles appear to be embedded in a surrounding network which can be attributed to be the amorphous part of the material. In comparison to sample 1 (Fig. 2, sample 1), slight differences can be seen for sample 3 (Fig. 2, sample 3), where the material appears to be coarser in the SEM-image. This is comparable to sample 6 (Fig. 2, sample 6), indicating that the coarser appearance occurs for samples with a high amount of zinc. As sample 8 is a mixture of samples 6 and 7 it was not analysed with SEM and EDX.

The EDX spectra correspond well to the findings from ICP-OES and confirm qualitatively as well as quantitatively the already made conclusions (the C peak in each EDX spectra originates from the sample holder).

Based on the findings from the undertaken characterisations, the appearance and composition of the samples can be summarised as follows:

Samples 1–5 have a rather similar structure and they all consist of crystalline particles embedded into a matrix of amorphous oxyhydroxides. A schematic is shown in Fig. 3a. This means that for these samples, although different in chemical composition, the structural composition is roughly the same. In sample 1, the crystalline part is zinc oxide and the amorphous part is a mixture of oxyhydroxides of the metal precursors Zn, Fe and Zr. A reduction of zinc (sample 2) or an increase of zirconia (sample 4) leads to the formation of zinc hydroxide as the crystalline part. In all cases, the initially precipitated material that did not contribute to the crystal formation is precipitated as amorphous oxyhydroxides. Furthermore it can be seen in the SEM-images that the two parts, crystalline particles and amorphous surrounding, are not separated but rather form a nanostructured composite. Samples 6 and 7 are different in appearance (see schematic Fig. 3b and c). Sample 6 consists solely of crystalline zinc oxide particles whereas sample 7 is composed of amorphous material, but in contrast to the samples 1–5, no zinc ions are incorporated in this matrix. Finally, since sample 8 is a mixture of the samples 6 and 7, it is composed of crystalline zinc oxide and an amorphous mixture of oxyhydroxides of iron and zirconia (see schematic Fig. 3d). As the two components (crystals and amorphous matter) are simply mixed after the synthesis, they are distinctly deposited next to each other but do not form an interconnected composite.

3.2 Adsorption behaviour of the synthesised materials towards phosphate

To verify qualitatively the successful phosphate adsorption on the material, FTIR spectroscopy measurements were conducted after P adsorption and compared to the material prior to adsorption (Fig. 4).

The FTIR spectroscopy results obtained from the pure samples reveal that samples 1–5 as well as sample 7 look very

Fig. 1 X-ray diffractograms of samples 1–7. Two different crystalline phases can be detected: zinc oxide is marked with "*" and zinc hydroxide is marked with "◊". The bars to the right represent the relative fraction of Zn (blue), Fe (red) and Zr (grey) in each sample.
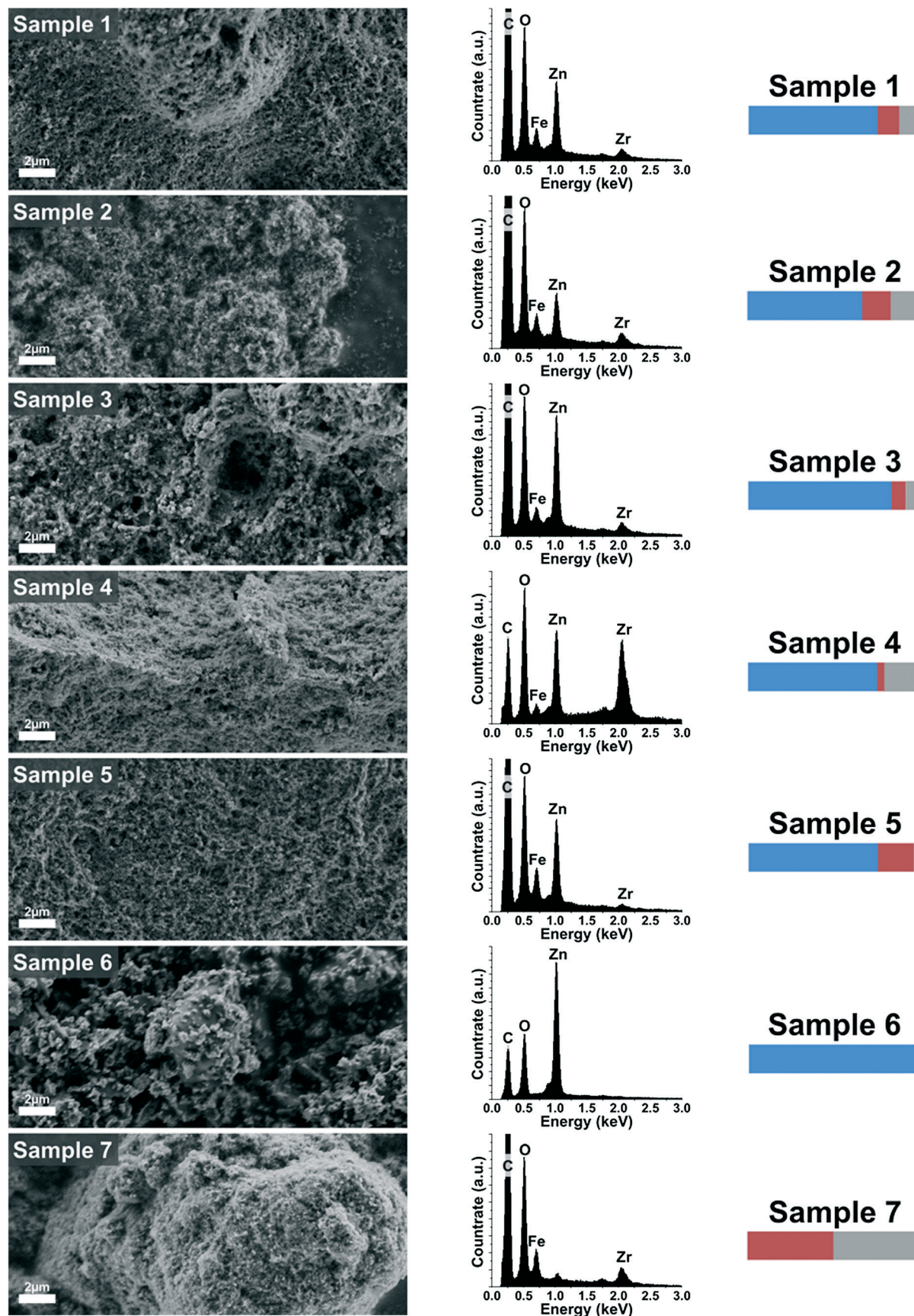
Fig. 2   SEM images of the samples 1–7 with the respective EDX-measurements. The bars to the right represent the relative fraction of Zn (blue), Fe (red) and Zr (grey) in each sample (the C peak in each EDX spectra originates from the sample holder).
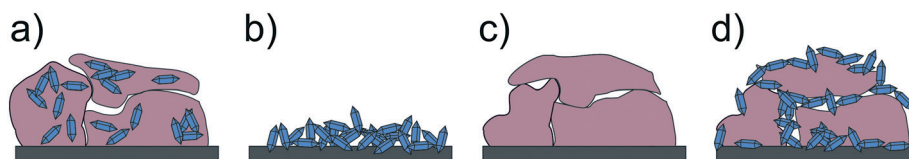
This journal is © The Royal Society of Chemistry 2017

Environ. Sci.: Nano, 2017, 4, 180–190 | 185

Fig. 3 Schematic depiction of the investigated samples. a) Samples 1–5, b) sample 6, c) sample 7 and d) sample 8.
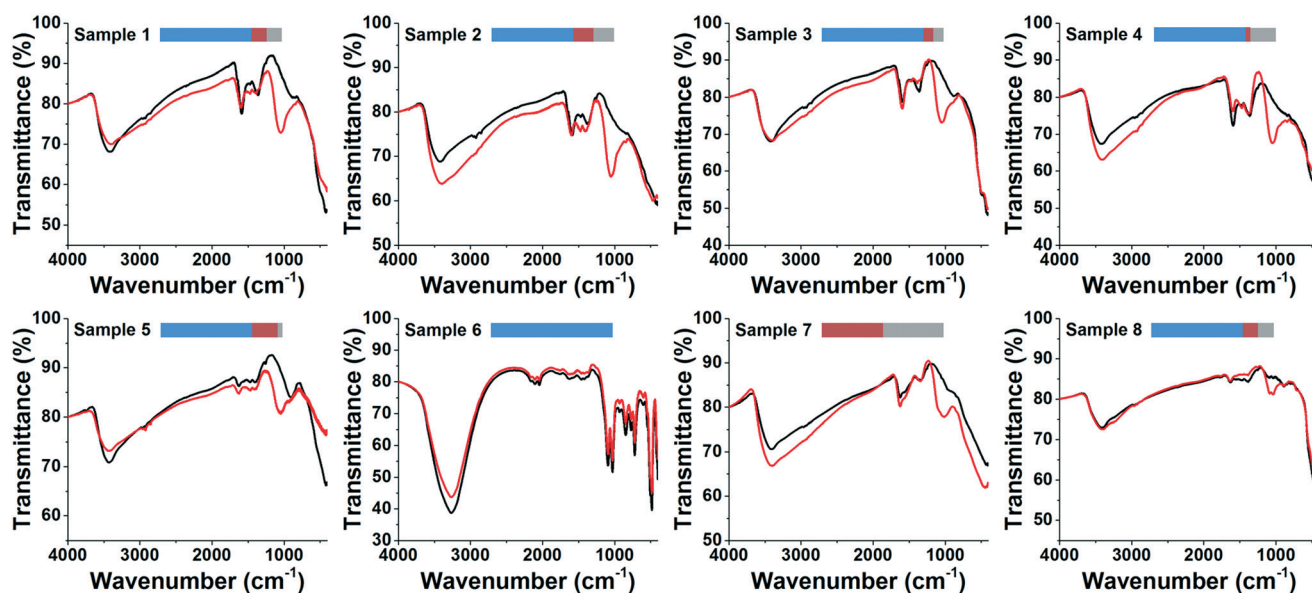
Fig. 4 Infrared spectra of pure (black line) and phosphate loaded (red line) samples. The bars represent the relative fraction of Zn (blue), Fe (red) and Zr (grey) in each sample.

similar (Fig. 4; black lines). Especially the group of IR absorption bands between 1750 and 1250 cm^{-1} is prominent. The band at about 1600 cm^{-1} can be attributed to scissors-bending of adsorbed water molecules.[28] The FTIR spectrograph of sample 6 does not show the absorption bands between 1750 and 1250 cm^{-1}, which are prominent in samples 1–5 (and 7). As sample 6 lacks Fe and Zr, the bands between 1750 and 1250 cm^{-1} can therefore be indirectly attributed to Fe and Zr hydroxide (M–OH) vibrations for the samples 1–5 (and 7). In addition, for sample 6, a series of bands is present in the range of 1250 to 400 cm^{-1}. These peaks can be attributed to ZnO. In the FTIR spectra obtained after the samples underwent phosphate adsorption (red graphs in Fig. 4), a new band appears at about 1050 cm^{-1} for most of the samples. This band is well-known from literature and can clearly be related to the asymmetric stretching vibrations of $H_nPO_4^{(3-n)-}$.[29,30] In our samples, this absorption band only appears in the spectra of the phosphate loaded samples, thus it can be clearly attributed to the adsorption of phosphate on the material. In sample 6, no evidence for this peak can be found, therefore implying that no or only negligible phosphate adsorption took place on this purely zinc containing material.

Adsorption kinetics measurements. Fig. 5 shows the phosphate uptake kinetics for each sample.

The phosphate adsorption occurs rapidly for all samples. After 10 min more than 95% of the total phosphate uptake measured after 1 hour is already detected. The experimental data were fitted both with pseudo-first-order and pseudo-second-order kinetic models. The pseudo-second-order model showed a very good compliance for all samples ($R^2 > 0.998$). The calculated parameters and regression coefficients for pseudo-first-order and pseudo-second-order kinetic models for all samples are summarized in Table S1 in the ESI.† The findings are in line with previous work done by us on the standard adsorber material and related structures and the kinetics modelling is discussed in more detail there.[24,25]

A comparison of the different curves reveals the influence of the employed metal salts. Starting from the standard sample 1, a decrease of zinc (sample 2) increases the phosphate uptake, whereas an increase of zinc (sample 3) decreases the phosphate uptake. Moreover, an increase of zirconia with the simultaneous decrease of iron (sample 4) leads to an increase in phosphate uptake and the opposite (increase of iron and decrease of zirconia, sample 5) results in lower phosphate uptake. The samples 6 and 7 represent the two extreme cases. Sample 6, which consists solely of zinc oxide, shows the lowest phosphate uptake of all samples. Sample 7 which contains no zinc but only iron and zirconia, shows the highest performance. A reason for these differences in phosphate
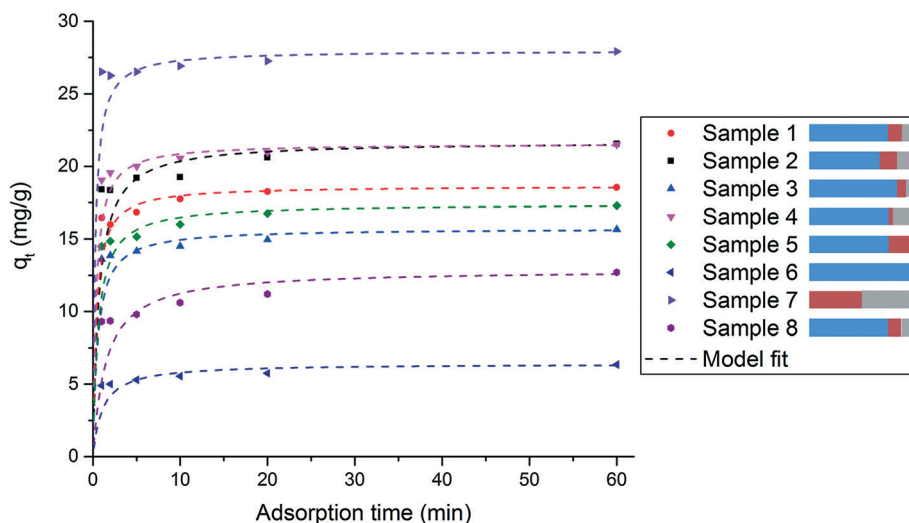
186 | *Environ. Sci.: Nano*, 2017, **4**, 180–190

This journal is © The Royal Society of Chemistry 2017

Fig. 5 Adsorption kinetics of phosphate on 200 mg L^{-1} adsorber. Initial PO$_4$-P concentration = 10 mg L^{-1}; q_t = amount of adsorbed phosphate in mg per gram adsorber at time t. A pseudo-second-order model is fitted to all experimental data sets. The bars to the right represent the relative fraction of Zn (blue), Fe (red) and Zr (grey) in each sample.

adsorption capacity could be attributed to the different specific surface areas of the samples (see Table 3). In fact for samples 1, 2 and 3 this would be a reasonable explanation, since both, the specific surface area and the adsorption capacity for phosphate correlate: the higher the surface area the higher and faster the P uptake. However, for samples 4 and 5 there is no direct correlation between specific surface area and phosphate uptake. These results reveal both the importance of zirconia for the phosphate uptake and the fact that an excessively high amount of zinc has a negative effect on the performance, suggesting that the binding of the phosphate is predominantly taking place in areas where zirconia is present. Nevertheless, for the later application as phosphate adsorber in real waste water, the presence of zinc is necessary because it is important for the adsorption selectivity towards phosphate over other competing anions in the waste water. This is not studied herein, however, it was exhaustively examined and discussed in other previous work by us.[24,25] A comparison of sample 1 with sample 8 (the sample that has the same composition as sample 1 but as a result of post-precipitation mixing and not simultaneous co-precipitation) reveals a significantly higher phosphate uptake for sample 1. Thus, the interconnected nanocomposite structure of crystalline and amorphous material, as it occurs by co-precipitation of all three metal cations, is crucial for better phosphate adsorption. Furthermore, this indicates that a synergetic effect prevails among the components of the material. This is very important for the phosphate uptake performance and cannot be generated by simply mixing the different components of the material after synthesis but can only be achieved by creating the nanostructure during synthesis.

XANES and EXAFS measurements. For a better understanding of the role that the metal ions play in the adsorption process, X-ray absorption fine structure (XAFS) spectro-

scopy was applied to selected samples with and without phosphate loading. The spectra were recorded at K-edges of all metal ions present in the samples, *i.e.* Fe, Zn and Zr. However, only in the case of iron K-edges and only for sample 1 significant changes of the spectra were observed upon phosphate loading. In Fig. 6 both the XANES and the EXAFS parts of the spectrum show a transition from an, at least partially, ordered local structure to an amorphous one. This is especially well visible in the EXAFS pattern of sample 1, where the peak of the second coordination shell almost completely disappears in the phosphate loaded phase. The XANES spectrum evolves into a spectral shape typical for iron in amorphous environment.[31] No shift of the absorption edge was observed, therefore the adsorption of the phosphate does not cause any change in the valency of the Fe ions. The Fe ions of sample 1 are present in the amorphous part together with Zr and Zn, whereas in the case of the other samples investigated with XAFS, Zn ions were not present in the vicinity of Fe. In these cases the local structure around the Fe ions was amorphous and no evolution in the structure was observed upon phosphate loading. Only some subtle alternations of the intensity of the white line were recognizable.

The XAFS measurements show that the presence of Zn ions in the amorphous part of the material close to the Fe ions is especially important. This indicates that crucial for the adsorption is not only the presence of zirconia but also of iron and zinc in the amorphous part of the material. These observations confirm once again that the interplay of all three metal ions in the nanostructure created upon synthesis is important for the adsorption to occur.

Adsorption isotherms measurements. Eventually, also the phosphate adsorption isotherms for all samples were acquired. A linear relationship between the dosed amount of particles and the adsorbed phosphate was observed at low
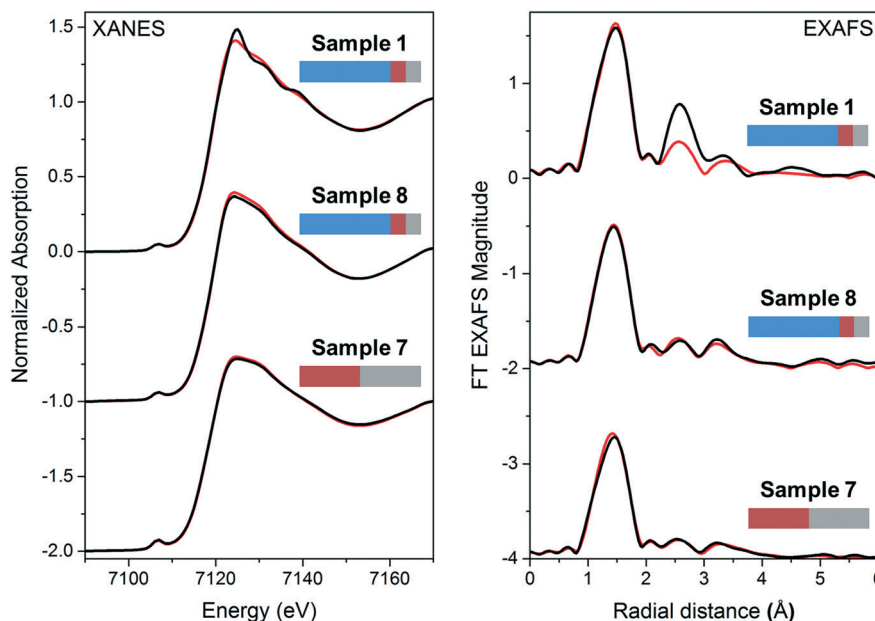
Fig. 6 (Left) XANES spectra of the particles measured at the K-edge of iron. (Right) Fourier transformed EXAFS patterns measured at the K-edge of iron. Spectra of particles loaded with phosphate are red and those of particles without phosphate loading are black. Only sample 1 shows significant changes in the spectral shape upon phosphate loading. The lack of well pronounced peaks beyond 2 Å in the EXAFS patterns indicates a strong structural disorder, *i.e.* amorphous structure.

adsorber concentrations, changing into an asymptotic convergence to nearly 100% adsorption at high adsorber concentrations (Fig. 7). At a concentration of 2000 mg L^{-1} adsorber, almost 100% of the phosphate was removed from the water (initial concentration of PO$_4$-P = 10 mg L^{-1}) with all samples, except for samples 6 and 8. This is in accordance with the results from the kinetics measurements, where these two samples showed the poorest performance.

The adsorption isotherms can be divided in two parts. At high adsorber concentrations and therefore lower equilibrium concentrations, the isotherms can be fitted by Lang-

muir and Freundlich models with good compliance and R^2-values between 0.938–0.990 for Langmuir and 0.915–0.996 for Freundlich. The only exception is sample 6 where the R^2-values are 0.094 and 0.455, respectively. The equation parameters generated for all samples are listed in Table S2 in the ESI.†

Interestingly, at lower adsorber concentrations, *i.e.* at higher equilibrium concentration, the isotherms show a BET-like adsorption behaviour indicating a multilayer adsorption on the surface of the material. An exception from this behaviour is sample 6. Since this material is a rather poor
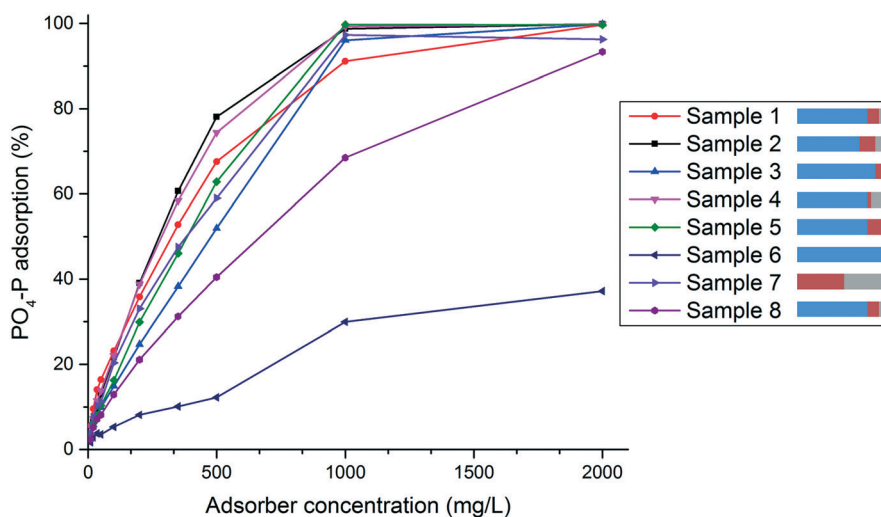

Fig. 7 Phosphate adsorption at equilibrium conditions for different amounts of adsorber material. The bars to the right represent the relative fraction of Zn (blue), Fe (red) and Zr (grey) in each sample.

188 | *Environ. Sci.: Nano*, 2017, **4**, 180–190

This journal is © The Royal Society of Chemistry 2017

phosphate adsorber, the BET-model fit did not render reasonable results and therefore a fitting with the BET-model was not possible. The equation parameters generated for the BET-model fit for all samples are also listed in Table S2 in the ESI.† In comparison to Freundlich and Langmuir, the R^2-values for the BET-model fit are lower (between 0.647–0.924). This could be expected since for the BET-fits all experimental data was used, unlike the Freundlich- and Langmuir- model fits where only data at low equilibrium concentration was considered.

The respective adsorption isotherms for each sample have similar appearances. Therefore, only the isotherm of sample 1 with the corresponding model fits is shown and discussed in detail here (Fig. 8). All other isotherms and the respective model fits can be seen in the ESI.†

Freundlich- and Langmuir-model fits for sample 1 show good match to the experimental data at low equilibrium concentrations C_e (see Fig. 8), however, at high equilibrium concentrations, the experimental data shows almost an exponential increase in phosphate uptake capacity. This part is in good compliance with the BET-model fit that is also shown in Fig. 8. With this information, the following assumption regarding the phosphate binding can be made:

Above a sample-specific adsorber concentration, all of the phosphate is adsorbed on the surface of the material. Moreover, at high adsorber concentration, the total specific surface area of the used material is large enough to capture all of the phosphate present in form of a monolayer on the surface. By providing a lower amount of adsorber, repulsive forces between adsorbed and dissolved phosphate-ions act against the further adsorption on the surface, still maintaining a monolayer on the material surface. A further reduction of adsorber leads to an almost exponential increase of adsorption capacity at higher equilibrium concentrations,
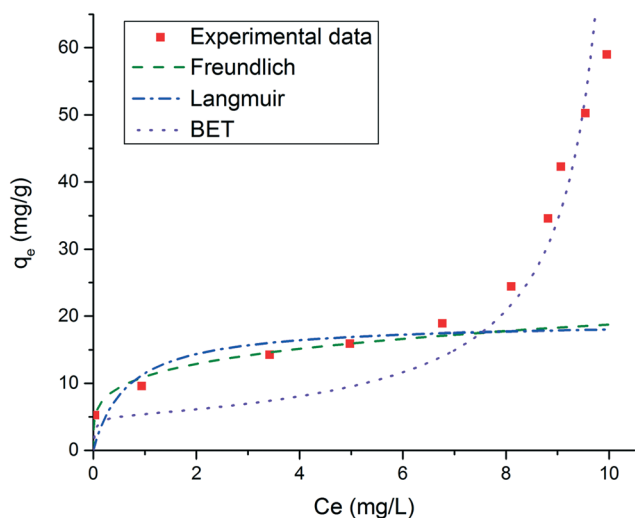
indicating a multilayer adsorption under these conditions. BET-like adsorption behaviour (multilayer adsorption) is well known for gases. However, although hardly known, it can also rarely be observed in fluids.[32] Interestingly, this BET-like adsorption behaviour also holds true for our material at high equilibrium concentrations. Another possible explanation for this adsorption behaviour could be a precipitation of metal phosphate such as $FePO_4$ which could occur after dissolution of Fe during adsorption. Since the adsorber material can be used in several adsorption–desorption cycles where phosphate is accumulated in a desorption solution, significant amounts of Fe should be found in this solution if such a precipitation was the reason for the phosphate uptake at the adsorber site. As our previous work showed that there is no significant accumulation of Fe in the desorption solution,[25] a precipitation of a metal phosphate is unlikely to take place.

4. Conclusion

The findings in this work indicate that the nanostructure of the ZnFeZr adsorber material has a crucial influence on its performance as phosphate adsorber. The material is composed of crystalline zinc oxide nanoparticles which are interconnected with an amorphous part consisting of zinc, iron and zirconia oxyhydroxides. This nanostructure which leads to significantly higher phosphate uptake can only be achieved by co-precipitation of the three metallic components and not by simply mixing the different components of the material after synthesis. This indicates that a synergetic effect prevails among the different components. We also found that the adsorption mechanism of phosphate on the adsorber material depends on the concentration of the adsorbate. As expected, at low concentrations monolayer adsorption takes place that can be described with Freundlich and Langmuir isotherm models. From the findings at high adsorbate concentrations however, a multilayer adsorption on the adsorber material is most likely.

Acknowledgements

Fig. 8 Phosphate adsorption isotherm of sample 1 at room temperature and pH 7–8 developed with Freundlich, Langmuir and BET models (q_e = amount of adsorbed phosphate in mg per gram adsorber at equilibrium; C_e = concentration of phosphate in the solution at equilibrium).

References

1 G. Tchobanoglous, F. L. Burton and H. D. Stensel, *Wastewater engineering. Treatment and reuse*, McGraw-Hill, Boston, 4th edn, 2003.

2 V. H. Smith, G. D. Tilman and J. C. Nekola, *Environ. Pollut.*, 1999, **100**, 179–196.

3 D. Cordell, J.-O. Drangert and S. White, *Global Environmental Change*, 2009, **19**, 292–305.

This journal is © The Royal Society of Chemistry 2017

Environ. Sci.: Nano, 2017, **4**, 180–190 | 189

4   D. Cordell, *8 reasons why we need to rethink the management of phosphorus resources in the global food system, the Story of P Information Sheet 1, Global Phosphorus Research Initiative, Institute for Sustainable Futures*, University of Technology, Sydney (UTS) Australia and Department of Water and Environmental Studies, Linkoeping University (LiU) Sweden, 2008.

5   S. Kentish, *Chem. Eng. J.*, 2001, **84**, 149–159.

6   E. Deliyanni, E. Peleka and N. Lazaridis, *Sep. Purif. Technol.*, 2007, **52**, 478–486.

7   R. Chitrakar, S. Tezuka, A. Sonoda, K. Sakane, K. Ooi and T. Hirotsu, *J. Colloid Interface Sci.*, 2006, **298**, 602–608.

8   J. Kim, W. Li, B. L. Philips and C. P. Grey, *Energy Environ. Sci.*, 2011, **4**, 4298.

9   Y.-J. Tu and C.-F. You, *Chem. Eng. J.*, 2014, **251**, 285–292.

10 M. A. H. Johir, M. Pradhan, P. Loganathan, J. Kandasamy and S. Vigneswaran, *J. Environ. Manage.*, 2016, **167**, 167–174.

11 Q. Liu, P. Hu, J. Wang, L. Zhang and R. Huang, *J. Taiwan Inst. Chem. Eng.*, 2016, **59**, 311–319.

12 N. Kawasaki, F. Ogata and H. Tominaga, *J. Hazard. Mater.*, 2010, **181**, 574–579.

13 S. Tanada, M. Kabayama, N. Kawasaki, T. Sakiyama, T. Nakamura, M. Araki and T. Tamura, *J. Colloid Interface Sci.*, 2003, **257**, 135–140.

14 M. Özacar, *Chemosphere*, 2003, **51**, 321–327.

15 D. Chandra and A. Bhaumik, *J. Mater. Chem.*, 2009, **19**, 1901.

16 A. Kugimiya and H. Takei, *Anal. Chim. Acta*, 2006, **564**, 179–183.

17 L. Lai, Q. Xie, L. Chi, W. Gu and D. Wu, *J. Colloid Interface Sci.*, 2016, **465**, 76–82.

18 W. Huang, Y. Zhu, J. Tang, X. Yu, X. Wang, D. Li and Y. Zhang, *J. Mater. Chem. A*, 2014, **2**, 8839.

19 R. S. S. Wu, K. H. Lam, J. M. N. Lee and T. C. Lau, *Chemosphere*, 2007, **69**, 289–294.

20 S. M. Ashekuzzaman and J.-Q. Jiang, *Chem. Eng. J.*, 2014, **246**, 97–105.

21 Y. Xu, Y. Dai, J. Zhou, Z. P. Xu, G. Qian and G. Q. M. Lu, *J. Mater. Chem.*, 2010, **20**, 4684.

22 K. Mandel, A. Drenkova-Tuhtan, F. Hutter, C. Gellermann, H. Steinmetz and G. Sextl, *J. Mater. Chem. A*, 2013, **1**, 1840–1848.

23 K.-H. Goh, T.-T. Lim and Z. Dong, *Water Res.*, 2008, **42**, 1343–1368.

24 A. Drenkova-Tuhtan, M. Schneider, K. Mandel, C. Meyer, C. Gellermann, G. Sextl and H. Steinmetz, *Colloids Surf., A*, 2016, **488**, 145–153.

25 A. Drenkova-Tuhtan, M. Schneider, M. Franzreb, C. Meyer, C. Gellermann, G. Sextl, K. Mandel and H. Steinmetz, *Water Res.*, 2017, **109**, 77–87.

26 Z. P. Xu, G. S. Stevenson, C.-Q. Lu, G. Q. M. Lu, P. F. Bartlett and P. P. Gray, *J. Am. Chem. Soc.*, 2006, **128**, 36–37.

27 B. Ravel and M. Newville, *J. Synchrotron Radiat.*, 2005, **12**, 537–541.

28 B. L. Mojet, S. D. Ebbesen and L. Lefferts, *Chem. Soc. Rev.*, 2010, **39**, 4643–4655.

29 Y. Arai and D. L. Sparks, *J. Colloid Interface Sci.*, 2001, **241**, 317–326.

30 W. E. Klee and G. Engel, *J. Inorg. Nucl. Chem.*, 1970, **32**, 1837–1843.

31 P. Stoch, W. Szczerba, W. Bodnar, M. Ciecinska, A. Stoch and E. Burkel, *Phys. Chem. Chem. Phys.*, 2014, **16**, 19917–19927.

32 P. Girods, A. Dufour, V. Fierro, Y. Rogaume, C. Rogaume, A. Zoulalian and A. Celzard, *J. Hazard. Mater.*, 2009, **166**, 491–501.